

An adaptive phase space method with application to reflection travelttime tomography

This article has been downloaded from IOPscience. Please scroll down to see the full text article.

2011 Inverse Problems 27 115002

(<http://iopscience.iop.org/0266-5611/27/11/115002>)

View [the table of contents for this issue](#), or go to the [journal homepage](#) for more

Download details:

IP Address: 35.10.92.179

The article was downloaded on 18/10/2011 at 18:36

Please note that [terms and conditions apply](#).

An adaptive phase space method with application to reflection traveltimes tomography

Eric Chung¹, Jianliang Qian², Gunther Uhlmann³ and Hongkai Zhao³

¹ Department of Mathematics, The Chinese University of Hong Kong, Hong Kong, People's Republic of China

² Department of Mathematics, Michigan State University, East Lansing, MI 48824, USA

³ Department of Mathematics, University of California, Irvine, CA 92697-3875, USA

E-mail: tschung@math.cuhk.edu.hk, qian@math.msu.edu, guhlmann@math.uci.edu and zhao@math.uci.edu

Received 25 November 2010, in final form 10 August 2011

Published 17 October 2011

Online at stacks.iop.org/IP/27/115002

Abstract

In this work, an adaptive strategy for the phase space method for traveltimes tomography (Chung *et al* 2007 *Inverse Problems* **23** 309–29) is developed. The method first uses those geodesics/rays that produce smaller mismatch with the measurements and continues on in the spirit of layer stripping without defining the layers explicitly. The adaptive approach improves stability, efficiency and accuracy. We then extend our method to reflection traveltimes tomography by incorporating broken geodesics/rays for which a jump condition has to be imposed at the broken point for the geodesic flow. In particular, we show that our method can distinguish non-broken and broken geodesics in the measurement and utilize them accordingly in reflection traveltimes tomography. We demonstrate that our method can recover the convex hull (with respect to the underlying metric) of unknown obstacles as well as the metric outside the convex hull.

(Some figures may appear in colour only in the online journal)

1. Introduction

Traveltimes tomography deals with the problem of determining the internal properties of a medium by measuring the traveltimes of waves going through the medium. It arises in global seismology in determining the inner structure of the Earth by measuring at different seismic stations the traveltimes of seismic waves produced by earthquakes. It also arises in exploration geophysics, in particular, hydrocarbon exploration. For instance, in marine reflection seismology, the data are collected on a ship with a streamer that sends out sound waves and receives the response on hydrophones or receiver groups.

Traveltime tomography also arises in medical imaging, in particular, in ultrasound computed tomography, in which the acoustic speed in biological tissues can be calculated from the arrival times of ultrasonic waves. Another area of application of traveltime tomography is ocean acoustics; see [33, 15, 7, 32] for related references.

Recent progress in boundary rigidity and lens rigidity problems in Riemannian geometry [17, 24, 35, 36, 48–53, 55] has motivated us to transfer these theoretical advances into numerical algorithms for recovering a Riemannian manifold; see [5, 6, 25, 26] for such algorithmic developments. In [5, 6], we have developed phase space methods for recovering such Riemannian manifolds in terms of the index of refraction in acoustic and isotropic elastic media from transmission traveltimes. In this paper, we incorporate an adaptive strategy into the phase space method and apply the resulting adaptive method to recovering the index of refraction from reflection traveltimes in an acoustic medium.

The problem of determining the Riemannian metric from first arrivals is known in differential geometry as the boundary rigidity problem. The traveltime information is encoded in the boundary distance function, which measures the distance, with respect to the Riemannian metric, between boundary points. The problem of determining the index of refraction from multiple arrival times is called the lens rigidity problem in differential geometry. The information is encoded in the scattering relation which gives the exit point and direction of a geodesic if we know the incoming point and direction plus also the travel time.

The boundary rigidity problem consists in determining a compact Riemannian manifold with boundary up to an action of a diffeomorphism which is the identity at the boundary by knowing the geodesic distance function between boundary points (see [51, 52] and references therein). One needs an *a priori* hypothesis to do so since it is easy to find counterexamples if the index of refraction is too large in certain regions. An *a priori* condition that has been proposed is the simplicity of the metric [31]. A manifold is simple if the boundary is strictly convex with respect to the Riemannian metric and there are no conjugate points along any geodesic. We remark that for simple manifolds, knowing the scattering relation is the same as knowing the boundary distance function. It is only for non-simple manifolds that the scattering relation gives more information including multiple arrival times. See [54, 55] for recent works for understanding conjugate points (caustics) and lens rigidity problems.

In [24], Kurylev, Lassas and Uhlmann have established a uniqueness result for recovering a compact Riemannian manifold from broken scattering relations. The essential idea in [24] is as follows: first, they impose some conditions on the broken scattering relation to verify whether a given family of geodesics intersect at one point; second, they show that the broken scattering relation determines the boundary distance representation of the Riemannian manifold, and the uniqueness follows from a certain isomorphism. However, the method of proof for the uniqueness result is not constructive. Another difficulty in practice is how to distinguish broken and non-broken scattering relations in the measurements. Here we propose a numerical reconstruction algorithm which is able to utilize both broken and non-broken scattering relations accordingly. First, we formulate the following simplified problem: how to reconstruct the index of refraction from reflection traveltimes based on given locations of reflectors, such as an embedded mirror inside the medium? Tacitly, we consider an incident ray path and its corresponding reflected ray path as a broken geodesic [24] with a reflection condition at the broken point. Next we consider the more challenging problem of generic reflection traveltime tomography in which an unknown reflector is buried in an unknown medium.

Numerically, since traveltime tomography has a long history of development, let us put our work into appropriate perspective. In terms of the source–receiver setup, traveltime tomography can be classified into transmission traveltime tomography, reflection traveltime

tomography or reflection plus transmission traveltime tomography [63, 12, 62, 11, 3, 1, 21, 34, 46, 47, 25]; see more references in the above citations. In terms of whether multipathing is allowed or not, traveltime tomography may be classified into first-arrival-based traveltime tomography [3, 4, 62, 1] or multi-arrival-based traveltime tomography [56, 14, 2, 5, 6, 26]. In terms of how the forward modeling is carried out in the implementation process, traveltime tomography may be classified into Lagrangian ray-tracing ODE-based traveltime tomography [63, 62, 11, 3, 4, 1, 21, 34] or Eulerian PDE-based traveltime tomography [46, 47, 25, 26]. In terms of media under consideration, traveltime tomography may be classified into isotropic or anisotropic traveltime tomography.

In general, ray-tracing-based first-arrival traveltime tomography is not robust because the ray path followed by ray tracing might not yield the least traveltime between a given source–receiver pair when there are multiple possible rays to connect the source–receiver pair in the presence of triplication and caustics. To develop a robust first-arrival-based traveltime tomography, one has to first develop robust forward modeling methods to generate reliable first-arrival traveltimes between a given source–receiver pair. Based on the contemporary viscosity-solution theory for Hamilton–Jacobi equations [27, 9, 10, 8], a lot of effort was devoted to developing fast and efficient eikonal solvers to compute first-arrivals for both isotropic [61, 37, 60, 43, 45, 38, 39, 64, 23, 41, 16, 29] and anisotropic media [13, 40, 59, 23, 42, 22]. Among these finite-difference eikonal solvers, the first-order fast marching and the first-order fast sweeping methods have proved to be unconditionally stable. Furthermore, related to the work in [46, 47], fast-sweeping-based eikonal solvers have been successfully used in isotropic transmission traveltime tomography in [25], and the resulting method is robust; this method has been further developed in [58, 57] for three-dimensional practical data.

As the first-arrival based traveltime tomography has limited resolution when the to-be-imaged structure is very complicated, it is desirable to develop a systematic formulation to utilize all the arrivals between a source–receiver pair. One question immediately comes up: how to parametrize all the arrivals between a source and receiver pair so that the information can be encoded into a rigorous mathematical formulation? To do that, one has to use a phase-space formulation so that multiple arrivals resulting from multipathing can be parametrized naturally by initial ray directions. In other words, one has to make use of the scattering relation to develop a rigorous mathematical framework. Such efforts have been made in [56, 14, 2, 5, 26, 6]. In [14], Delprat-Jannaud and Lailly have developed a phase-space approach to parametrize multi-arrival traveltimes by using the receiver location and the ray parameter at the receiver, and their implementation is based on Lagrangian ray-tracing ODE methods for forward modeling. In [26], Leung and Qian have developed a Liouville-equation-based PDE approach for carrying out traveltime tomography which is able to utilize all arrivals. In [2], Billette and Lambare have developed a phase-space approach which makes full use of the scattering relation; however, the proposed model in [2] is not well justified yet as it includes not only the velocity (the metric) but also other parameters.

In [5, 6], the authors have developed a systematic phase-space approach for traveltime tomography for acoustic and elastic media by using the Stefanov–Uhlmann identity (11) formulated in [49]. The advantages of the approach in [5, 6] are multifold. As a first advantage, multipathing can be taken into account systematically, as evidenced in [14, 26] and in numerical examples shown later. As demonstrated in [18, 28], multipathing is essential for high resolution seismic imaging. As a second advantage, our phase space formulation has the potential to recover generic (anisotropic) Riemannian metrics. These advantages distinguish our new method from other traditional methods in inverse kinematic problems [3, 44, 46, 47, 4, 62, 25] in that those traditional methods only recover isotropic metrics by using first-arrivals.

Moreover, our numerical algorithm is based on a hybrid approach. A Lagrangian formulation (ray tracing) is used in phase space for the linearized Stefanov–Uhlmann identity (12). This allows us to deal with multipathing naturally. On the other hand, an Eulerian formulation is used for the index of refraction of the medium. As a consequence our computational domain is in physical space rather than in phase space, which reduces the degree of freedom and hence the computational cost.

Because the Stefanov–Uhlmann identity is posed in phase space, we have to find a way to pick the data that are in phase space, and such data are not measurable directly. To do that we recall that in kinematic inverse problems, the data used frequently are traveltimes data, which means that traveltimes can be parametrized by source locations and ray parameters; in turn, ray parameters can be derived from the eikonal equation and the traveltimes data as illustrated in [30, 20, 56, 26]. Therefore, without any hesitation, we use the identity as our foundation to carry out the inversion process.

The Stefanov–Uhlmann identity is also related to the so-called Liouville equation, but the current formulation is different from the one used in [26]. In that work [26], Leung and Qian formulated the inverse problem for isotropic metrics in an Eulerian framework and used an adjoint state method to minimize a mismatching functional. The current new formulation is based on a novel identity to cross-correlate the information from two metrics so that the two metrics can pass information to each other at every stage.

In this work, we improve the phase space method developed in [5] by incorporating an adaptive strategy into the formulation. Although the Stefanov–Uhlmann identity (11), which links two metrics and their corresponding scattering relations together, is valid in a quite general setting, the identity is truly nonlinear in terms of the two metrics. It is essential that the two metrics are close to each other in both mathematical analysis and numerical computation (through linearization). For the phase space method proposed in [5], all geodesics are used simultaneously based on the linearized Stefanov–Uhlmann identity (12) at each step. First, this creates a large linear system that involves the unknowns in the computational domain. Second, when an initial guess of the metric is poor, using predicted geodesics that are far from the true ones may lead to too many iterations or even make the iterative procedure diverge. The key idea of the adaptive approach is to first utilize those geodesics that match the measurements well under the current metric. For example, geodesics that are short enough and close to the boundary can always match the data well. This is because the metric near the boundary is close to the metric at the boundary which is known. We then use the hybrid phase space method restricted to these geodesics to improve/recover the metrics in the neighborhood of these geodesics in the physical space. As a result of the improved approximation of the metric in a certain part of the domain, more geodesics will match with the measurements better and will be used in the next step. If we continue with the process, more geodesics will be used so that one can recover the metrics in larger regions of the domain. The adaptive approach improves stability by using only those more accurate geodesics at each step. It also improves efficiency by gradually involving more and more unknowns in a stable fashion. A physical analog could be in the spirit of layer stripping. Initially short geodesics which are usually close to the boundary are used to provide a good estimate of the metric in a boundary layer. Then, longer geodesics are used and the boundary layer of good estimate expands further into the interior. Of course the crucial point is that we do not have to specify the layers physically which is impossible without knowing the underlying metric. Instead we use data matching to automatically pick geodesics sequentially and our hybrid phase space method can recover the underlying metric in the neighborhood of the picked geodesics in physical space. Also geodesics that match data well may not be short ones. We then apply this adaptive phase space method to reflection tomography where broken geodesics/rays have to be taken into account.

In particular, a jump condition of the geodesic flow in the phase space has to be enforced at the broken point and the Stefanov–Uhlmann identity has to be modified accordingly. More importantly our adaptive strategy can effectively distinguish and utilize measurements from non-broken and broken geodesics accordingly.

The paper is organized as follows: we introduce the formulation for reflection traveltime tomography and broken geodesics in section 2. Then, we present the numerical algorithm and the adaptive approach in section 3. Numerical examples are presented in section 4.

2. Mathematical formulation for reflection traveltime tomography

2.1. Broken scattering relation

Consider a compact Riemannian manifold (M, g) with a boundary of dimension n . Let SM denote its unit tangent bundle. Then, we can introduce the following scattering relation or lens relation [19, 31]:

$$\mathcal{L} = \{(x, \xi), (y, \zeta), t) \in SM \times SM \times \mathbb{R} : x, y \in \partial M, \\ (\gamma_{x,\xi}(t), \partial_t \gamma_{x,\xi}(t)) = (y, \zeta) \text{ for some } t \geq 0\},$$

where $\gamma_{x,\xi}$ is the geodesic of (M, g) that leaves from x to direction ξ at $t = 0$.

As defined in [24], a broken geodesic (or, a once broken geodesic) is a path $\alpha = \alpha_{x,\xi,z,\eta}(t)$, where $z = \gamma_{x,\xi}(s) \in M$ for some $s \geq 0$, $\eta \in S_z M$, and

$$\alpha_{x,\xi,z,\eta}(t) = \begin{cases} \gamma_{x,\xi}(t) & \text{for } t < s, \\ \gamma_{z,\eta}(t-s) & \text{for } t \geq s. \end{cases} \quad (1)$$

Accordingly, the boundary entering and exiting points of broken geodesics define the broken scattering relation [24]

$$\mathcal{R} = \{(x, \xi), (y, \zeta), t) \in SM \times SM \times \mathbb{R}_+ : (x, \xi) \in \Omega_+, (y, \zeta) \in \Omega_-, t = \ell(\alpha_{x,\xi,z,\eta}), \\ \text{and } (\alpha_{x,\xi,z,\eta}(t), \partial_t \alpha_{x,\xi,z,\eta}(t)) = (y, \zeta) \text{ for some } (z, \eta) \in SM\},$$

where $\ell(\alpha_{x,\xi,z,\eta}) \in \mathbb{R}_+ \cup \{\infty\}$ denotes the smallest $\ell > 0$ such that $\alpha_{x,\xi,z,\eta}(\ell) \in \partial M$, ν denotes the interior unit normal vector of M which is used to define the following incoming and outgoing boundary directions:

$$\Omega_+ = \{(x, \xi) \in SM : x \in \partial M, (\xi, \nu)_g > 0\}, \\ \Omega_- = \{(x, \xi) \in SM : x \in \partial M, (\xi, \nu)_g < 0\}.$$

We remark that the broken scattering relation does not contain information about the point z where the broken geodesic $\alpha_{x,\xi,z,\eta}$ changes its direction [24].

The uniqueness result proved in [24] is not constructive. Therefore, we are interested in developing a numerical algorithm to utilize the broken scattering relation in a systematic way.

2.2. Mathematical formulation

Let Ω be a bounded domain in \mathbb{R}^n and let (g_{ij}) be a Riemannian metric defined on it. Following [5, 6], we define the Hamiltonian H_g by

$$H_g(x, \xi) = \frac{1}{2} \left(\sum_{i,j=1}^n g^{ij}(x) \xi_i \xi_j - 1 \right) \quad (2)$$

for each $x \in \Omega$ and $\xi \in \mathbb{R}^n$. In the above definition $(g^{ij}) = (g_{ij})^{-1}$ is the inverse of the matrix (g_{ij}) . Let $X^{(0)} = (x^{(0)}, \xi^{(0)})$ be a given initial condition from the following inflow set:

$$\mathcal{S}^- = \left\{ (x, \xi) \mid x \in \partial\Omega, H(x, \xi) = 1, \sum_{i,j=1}^n g^{ij}(x) \xi_i v_j(x) < 0 \right\},$$

where $v(x)$ is the unit outward normal vector of $\partial\Omega$ at the point x and $v_j(x)$ denotes the j th component of this vector. We define $X_g(s, X^{(0)}) = (x(s), \xi(s))$ by the solution of the following system:

$$\frac{dx}{ds} = \frac{\partial H_g}{\partial \xi}, \quad \frac{d\xi}{ds} = -\frac{\partial H_g}{\partial x} \quad (3)$$

with the initial condition

$$(x(0), \xi(0)) = X^{(0)}.$$

We suppress the dependence of $(x(s), \xi(s))$ on $X^{(0)}$. The solution X_g defines a geodesic/ray in the phase space, parametrically via $x(s)$, in the physical space Ω with the co-tangent vector $\xi(s)$ at any point $x(s)$. The parameter s denotes traveltime.

In this paper, we consider the case when there are obstacles inside the domain Ω . In this case, the ray will be reflected at the boundary of the obstacles. Mathematically, we need to impose the jump condition for the above system (3). For simplicity, we will derive the jump condition for the case when there is only one obstacle lying strictly inside Ω and the ray intersects the obstacle at most once. Let Γ be the interface where the ray will be reflected. Note that there is a unique time $s^* > 0$ such that the point $x(s^*)$ hits the interface at an incoming angle defined by $\xi_{\text{in}} := \xi(s^*)$. The ray will be reflected at an outgoing angle defined by $\xi_{\text{out}} = R(\xi_{\text{in}}; x(s^*))$ which is specified by the normal vector of Γ at the point $x(s^*)$ according to the law of reflection in geometrical optics. We remark that the function R depends on the contact point $x(s^*)$.

Thus, the vector $X_g(s, X^{(0)})$ is defined as follows:

$$\frac{dx}{ds} = \frac{\partial H_g}{\partial \xi}, \quad \frac{d\xi}{ds} = -\frac{\partial H_g}{\partial x}, \quad 0 < s < s^*, \quad (x(0), \xi(0)) = X^{(0)} \quad (4)$$

and

$$\frac{dx}{ds} = \frac{\partial H_g}{\partial \xi}, \quad \frac{d\xi}{ds} = -\frac{\partial H_g}{\partial x}, \quad s > s^*, \quad (x(s^*), \xi(s^*)) = (x(s^*), \xi_{\text{out}}). \quad (5)$$

In the derivation below, we will need the Jacobian matrix

$$J_g(s, X^{(0)}) := \frac{\partial X_g}{\partial X^{(0)}}(s, X^{(0)}) = \begin{pmatrix} \frac{\partial x}{\partial x^{(0)}} & \frac{\partial x}{\partial \xi^{(0)}} \\ \frac{\partial \xi}{\partial x^{(0)}} & \frac{\partial \xi}{\partial \xi^{(0)}} \end{pmatrix} \quad (6)$$

which is the derivative of X_g with respect to the initial condition $X^{(0)}$. Let

$$M = \begin{pmatrix} H_{\xi,x} & H_{\xi,\xi} \\ -H_{x,x} & -H_{x,\xi} \end{pmatrix}. \quad (7)$$

Then, we have

$$\frac{dJ}{ds} = MJ, \quad J(0) = I \quad \text{for } 0 < s < s^*, \quad (8)$$

and

$$\frac{dJ}{ds} = MJ, \quad J(s^*) = B \quad \text{for } s > s^*, \quad (9)$$

where

$$B = \begin{pmatrix} J(s^*)_{11}, & J(s^*)_{12} \\ R_\xi(\xi_{\text{in}}; x(s^*))J(s^*)_{21} + R_x(\xi_{\text{in}}; x(s^*))J(s^*)_{11}, & R_\xi(\xi_{\text{in}}; x(s^*))J(s^*)_{22} + R_x(\xi_{\text{in}}; x(s^*))J(s^*)_{12} \end{pmatrix}. \quad (10)$$

Next we will derive the broken Stefanov–Uhlmann identity. Similar to [49, 5], we define

$$F(s) = X_{g_2}(t - s, X_{g_1}(s, X^{(0)})),$$

where $t = t_{g_1}$. Then, we have

$$\int_0^t F'(s) \, ds = X_{g_1}(t, X^{(0)}) - X_{g_2}(t, X^{(0)}).$$

The time integral on the left-hand side is

$$\int_0^t F'(s) \, ds = \int_0^t \frac{\partial X_{g_2}}{\partial X^{(0)}}(t - s, X_{g_1}(s, X^{(0)})) \times (V_{g_1} - V_{g_2})(X_{g_1}(s, X^{(0)})) \, ds.$$

Hence, we have the Stefanov–Uhlmann identity

$$X_{g_1}(t, X^{(0)}) - X_{g_2}(t, X^{(0)}) = \int_0^t J_{g_2}(t - s, X_{g_1}(s, X^{(0)})) \times (V_{g_1} - V_{g_2})(X_{g_1}(s, X^{(0)})) \, ds. \quad (11)$$

Linearizing the right-hand side at g_2 , we have

$$X_{g_1}(t, X^{(0)}) - X_{g_2}(t, X^{(0)}) \approx \int_0^t J_{g_2}(t - s, X_{g_2}(s, X^{(0)})) \times \partial_{g_2} V_{g_2}(g_1 - g_2)(X_{g_2}(s, X^{(0)})) \, ds. \quad (12)$$

In the case of an isotropic medium

$$g_{ij} = \frac{1}{c^2} \delta_{ij}, \quad \partial_g V_g(\lambda) = (2c\lambda\xi, -(\lambda\nabla c + c\nabla\lambda)|\xi|^2).$$

Moreover, we have the following group property:

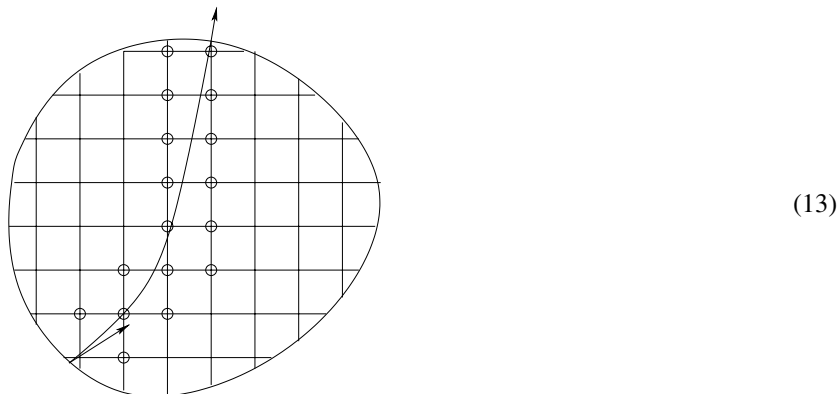
$$J_{g_2}(t - s, X_{g_2}(s, X^{(0)})) = J_{g_2}(t, X^{(0)})J_{g_2}(s, X^{(0)})^{-1}.$$

3. Adaptive phase space method

3.1. The phase space method

We first introduce the general setup of the phase space method for traveltimes tomography proposed in [5]. The numerical method is an iterative algorithm based on the linearized Stefanov–Uhlmann identity (12) using a hybrid approach. The metric g is defined on an underlying Eulerian grid in the physical domain. The integral equation (12) is discretized along a ray for each $X^{(0)}$ in phase space. The Jacobian matrix along the ray is computed according to (8) (and (9), (10) for broken rays). On the ray, values of g are computed by interpolation from the neighboring grid point values. Hence, each integral equation along a particular ray yields a linear equation for grid values of g in the neighborhood of the

ray in the physical domain (see the below diagram). Here is the iterative algorithm for finding g .



Let $X_i^{(0)}, i = 1, 2, \dots, m$, be the initial locations and directions of those m measurements (scattering relations) $X_g(t_i, X_i^{(0)})$ where t_i is the exit time corresponding to the i th geodesic starting at $X_i^{(0)}$. Starting with an initial guess of the metric g^0 , we construct a sequence g^n as follows.

Define the mismatch vector

$$d_i^n = X_g(t_i, X_i^{(0)}) - X_{g^n}(t_i, X_i^{(0)})$$

and a linear operator based on (12) along the i th geodesic

$$K_i^n g = \int_0^{t_i} J_{g^n}(t_i - s, X_{g^n}(s, X_i^{(0)})) \times \partial_{g^n} V_{g^n}(g)(X_{g^n}(s, X_i^{(0)})) ds. \tag{14}$$

Note that both d_i^n and K_i^n depend on $X_i^{(0)}$. Then, for each $n \geq 0$, we find \tilde{g} that minimizes

$$F(g) = \frac{1}{2} \sum_{i=1}^m \|K_i^n g - d_i^n\|^2 + \frac{\beta}{2} \|\nabla g\|_{L^2(\Omega)}^2, \tag{15}$$

where the last term is a regularization term since the inverse problem is ill-posed and the resulting linear system may not have a unique solution. The choice of β may depend on the noise level and scale of the problem. We then define

$$g^{n+1} = g^n + \tilde{g}.$$

3.2. An adaptive strategy

In the original phase space method, all rays from the measurements are used at the same time for the reconstruction; see equations (14) and (15). It results in a large linear system. Moreover, the use of geodesics that are far from the true ones may make the linearization-based iterative algorithm converge slowly with more iterations or even make the algorithm diverge. So we propose the following adaptive strategy. At each step, we pick up those geodesics in the current metric that produce small mismatch with the measurements, i.e. the scattering relations. Then, we apply the phase space method only to these geodesics which will provide a good approximation of the true metric in the neighborhood of those picked geodesics. Then, the improvement of the current metric will result in more geodesics that have a small mismatch with measurements; in turn, this allows us to recover the metric in a larger region in the next step.

Here is the adaptive algorithm that we propose in our numerical implementation. For each n , we will use D_n to represent a subset of $\{1, 2, \dots, m\}$. The set D_n contains all indices i such that the mismatch data d_i^n are small enough. More precisely, for a given tolerance $\varepsilon > 0$, we define

$$D_n = \left\{ i \mid \frac{\|d_i^n\|}{\|X_g(t_i, X_i^{(0)}) - X_i^{(0)}\|} < \varepsilon \right\},$$

where the mismatch is normalized by the difference between the starting location and ending location for each geodesic in the phase space, which can be obtained directly from the measurements. Then, for each $n \geq 0$, we find \tilde{g} that minimizes

$$F(g) = \frac{1}{2} \sum_{i \in D_n} \|K_i^n g - d_i^n\|^2 + \frac{\beta}{2} \|\nabla g\|^2.$$

We then define

$$g^{n+1} = g^n + \tilde{g}.$$

In practice, we will choose ε to be proportional to the sum of the normalized mismatch σ_n defined by

$$\sigma_n = \sum_{i=1}^m \frac{\|d_i^n\|}{\|X_g(t_i, X_i^{(0)}) - X_i^{(0)}\|}.$$

This adaptive strategy has some flavor of a layer-stripping method in the sense that shorter geodesics that are closer to the boundary usually give smaller mismatch and are used at an earlier stage to recover/improve the metric near boundary. This is because the metric near the boundary is close to the metric at the boundary which is known. However, the crucial difference is that our method does not need to define layers explicitly in physical space and is done automatically based on data. This adaptive approach improves robustness, efficiency and accuracy in comparison to using all geodesics simultaneously.

Moreover, the adaptive strategy can distinguish and use broken geodesics and non-broken geodesics in the measurements, which is important for reflection travel time tomography. On the one hand, if the obstacle or the reflection interface is inside the domain, using broken geodesics only may be unstable since there may be no short broken geodesics that is a small perturbation of the true one. On the other hand, using non-broken geodesics only can at most recover the metric outside the convex (with respect to the metric) hull of the obstacle. Nevertheless, our adaptive strategy can distinguish broken and non-broken geodesics when both are present in the measurements; if we predict a broken or non-broken geodesic erroneously, it will produce a large error ($O(1)$) in the scattering relation due to the jump condition (10) at the broken point. Hence, incorrectly predicted geodesics will not be used in the reconstruction. In practice, the adaptive strategy will likely pick up those non-broken and short geodesics that provide small mismatch and recover the metric in a region close to the boundary first. Then, more geodesics, including broken ones, will be picked up so that larger regions, including the concave region, will be covered. These observations are verified by numerical results in the next section. Actually we show that we can use geodesics that are broken multiple times numerically. In the most challenging situation where neither the obstacle nor the underlying metric is known, our adaptive method can pick up most non-broken geodesics during the reconstruction. As a result (see example 4.6 below) we recover (1) the convex hull of the unknown obstacle given by the envelope of used non-broken geodesics and (2) the metric outside the convex hull. An interesting problem for future study is how to improve the reconstruction using broken geodesics based on the result from non-broken ones. The main challenge is how to represent the geometry of the envelope of the used non-broken geodesics to predict the broken points and jump conditions for broken geodesics.

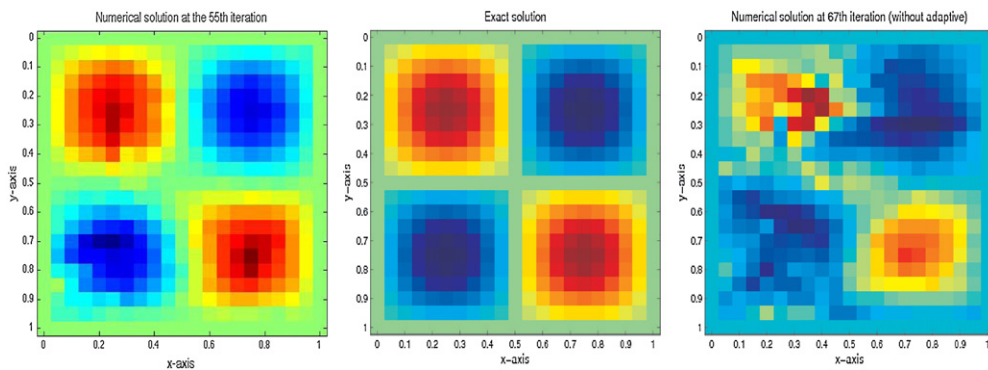


Figure 1. Left: numerical solution (using adaptive) at the 55th iteration. Middle: exact solution. Right: numerical solution (without adaptive) at the 67th iteration.

Remark. In general, our approach can stably recover metrics in regions where measured geodesics cover. Moreover, in regions where there are shorter geodesics the reconstruction is more accurate. This phenomenon will be demonstrated by using partial data in example 3 in the next section.

Finally, we will briefly discuss the cost of computation of our new method. For each iteration, we will need to solve the ODEs (4) and (5) for each source datum. These solutions are then saved in the memory and our new adaptive method will pick up a subset of them for the computation of K_i^n . The resulting symmetric and positive definite linear system, which has a dimension equal to the number of unknowns of the Eulerian grid, is then solved by standard solvers.

4. Numerical experiments

In this section, we use numerical experiments to show the effectiveness and robustness of our adaptive approach in various setups.

4.1. Example 1: an example without broken geodesics

The purpose of this example is to compare the reconstruction obtained by using all geodesics simultaneously (the original phase space method proposed in [5]) with that obtained by the adaptive strategy proposed in this work.

The exact solution is $c(x, y) = 1 + 0.3 \sin(2\pi x) \sin(2\pi y)$. The initial guess is $c_0(x, y) = 0.8$. The grid size is 20×20 and we use 200 directions at each grid point on only one side of the boundary $\{y = 0\}$. The regularization parameter is taken as $\beta = 0.1$.

In the adaptive approach, we take $\varepsilon = 0.25\sigma_n$. The algorithm converges to a solution with a relative error 1.3×10^{-2} at the 55th iteration. We plot numerical and exact solutions in the left plot and the center plot of figure 1, respectively. We see that we obtain a good recovery of the unknown function $c(x, y)$.

Without the adaptive strategy, the algorithm converges at the 67th iteration with a relative error 4.4×10^{-2} . The numerical solution in this case is shown in the right plot of figure 1.

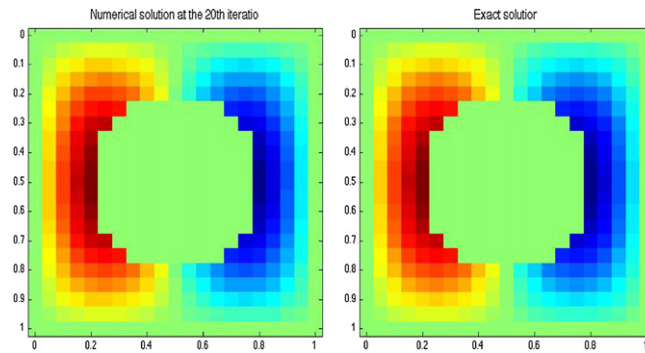


Figure 2. Left: numerical solution at the 20th iteration. The relative error is 0.094%. Right: exact solution.

4.2. Example 2: a known circular obstacle enclosed by a square domain

We consider a known circular obstacle with boundary Γ being a circle with center $(0.5, 0.5)$ and radius 0.3. In this example, the geodesic either does not hit the inclusion (non-broken) or hits the inclusion (broken) once.

The exact solution is $c(x, y) = 1 + \frac{1}{5} \sin(2\pi x) \sin(\pi y)$. The initial guess is $c_0(x, y) = 0.8$. The grid size is 20×20 and we use 100 incoming directions at each grid point on the boundary. We also add 5% noise to the data. The regularization parameter is taken as $\beta = 10^{-4}$. For the parameter of the adaptive strategy, we take $\varepsilon = 0.5\sigma_n$. The algorithm converges to a solution with a relative error 9.4×10^{-4} at the 20th iteration. We plot the numerical and exact solutions in figure 2, respectively.

4.3. Example 3: a circular domain

We consider the case when the domain Ω is a circle which is centered at $(0.5, 0.5)$ with radius 0.4.

The exact solution is $c(x, y) = 1 + 0.3 \cos(r)$ where $r = \sqrt{(x - 0.5)^2 + (y - 0.5)^2}$. The initial guess is $c_0(x, y) = 0.6$. The grid size is 40×40 . We choose 30 source points which are uniformly distributed on the boundary of Ω and at each source point we use 101 incoming directions. The regularization parameter $\beta = 10^{-3}$. For the parameter of the adaptive process, we take $\varepsilon = 0.05\sigma_n$.

The numerical results of the first six iterations are shown in figure 3. The ray coverage for the first six iterations are shown in figure 4. The number of rays used are 478, 620, 900, 1117, 1406 and 1625, respectively. We can see that the adaptive strategy picks up mostly short geodesics first. As the iteration goes on, more and more geodesics are picked up that cover larger and larger regions to update the metric.

In figure 5, we have shown both the numerical solution at the 13th iteration and the exact solution. The two match with each other very well with a relative error of 0.01%.

4.4. Example 4: partial data

With the same setting as above, we will test our numerical algorithm with limited data source on the boundary. In the first case, we put sources only on the upper half of the circular domain, while in the second case, we distribute sources only on the upper-right quarter of the

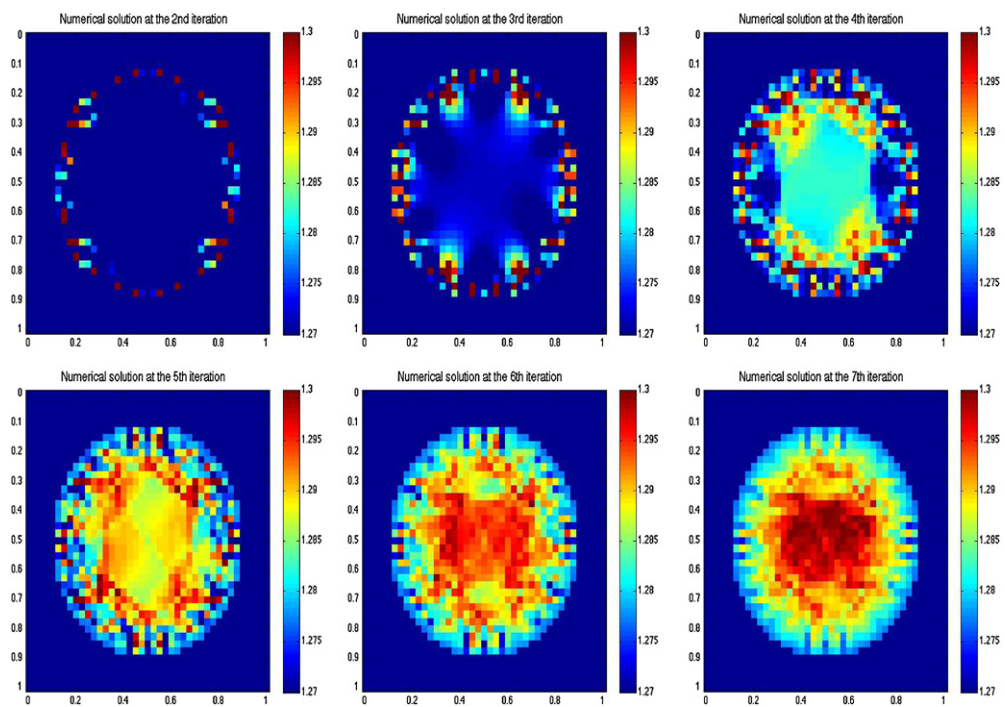


Figure 3. Numerical solutions from the second to the seventh iterations.

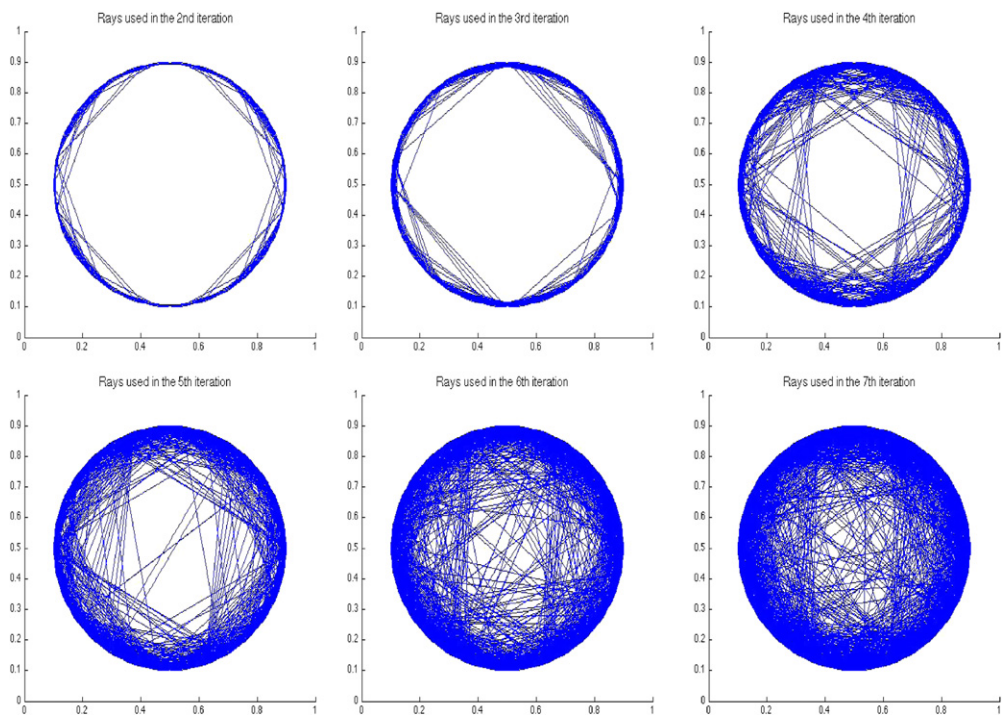


Figure 4. Rays used from the second to the seventh iterations.

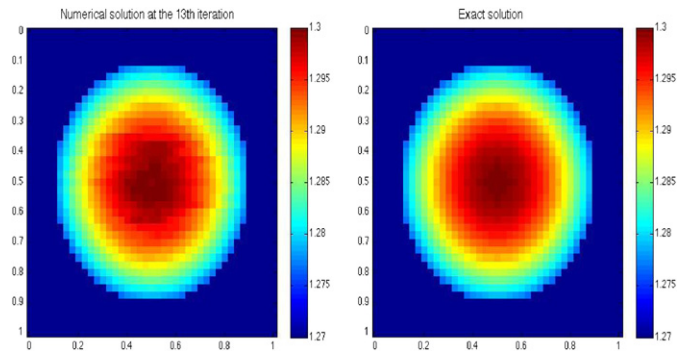


Figure 5. Left: numerical solution at the 13th iteration. Right: exact solution.

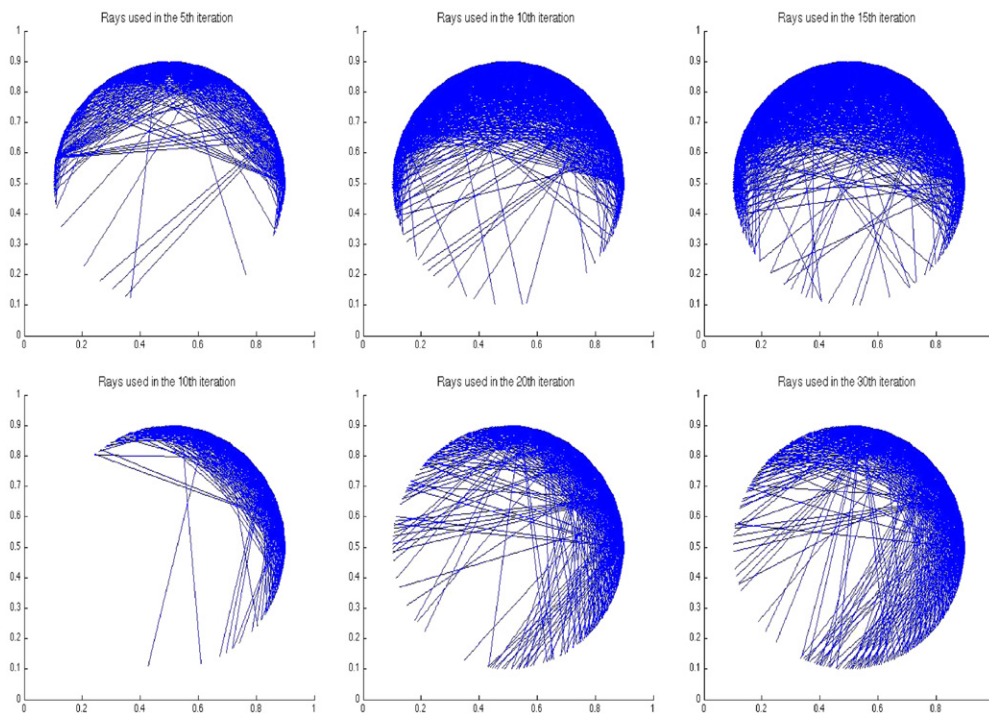


Figure 6. Top: rays used in the 5th, 10th and 15th iterations for data source on the upper part of the domain. Bottom: rays used in the 10th, 20th and 30th iterations for data source on the upper-right part of the domain.

circular domain. Measurements are taken at the whole boundary. In these cases, our adaptive approach uses those shorter geodesics and recovers metrics that are close to the boundary part where sources are distributed in the beginning iterations, and then gradually uses those longer geodesics and recovers metrics further away from the sources. This is shown in figure 6. In figure 7, we also plot the rays used at convergence. As explained before, in regions where shorter geodesics exists, such as near the source locations, the reconstruction is better. This is

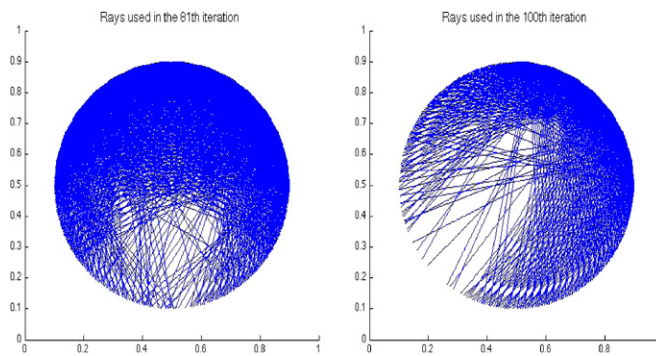


Figure 7. Left: rays used with data source on the upper part of the circular domain for the 81st iterate. Right: rays used with data source on the upper-right part of the circular domain for the 100th iterate.

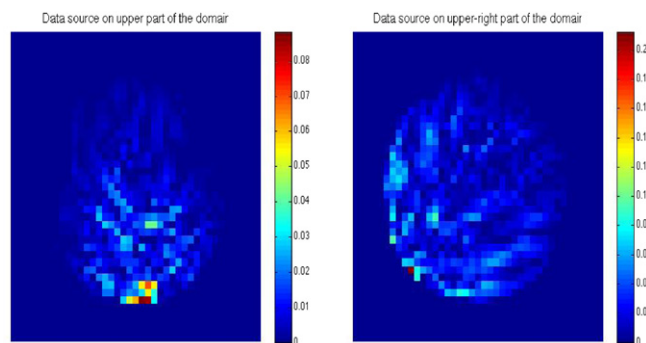


Figure 8. Left: relative error with data source on the upper part of the circular domain for the 81st iterate. Right: relative error with data source on the upper-right part of the circular domain for the 100th iterate.

confirmed by the results shown in figure 8, where the relative errors for the above two cases are illustrated. Another observation is that the relative error for the first case is smaller than that of the second case due to the obvious fact that there are more data in the first case.

Next we test two cases where sources are placed on the upper half of the boundary while the measurements are obtained on the upper half of the boundary and the lower half of the boundary, respectively. In figure 9, we show the absolute errors for these two tests. We see that the errors are typically smaller in regions closer to the domain boundary where measurements are taken. Rays used throughout the iterations are shown in figure 10. Again we see that shorter rays are used at the beginning and more rays are gradually used as iteration proceeds. For the case with data obtained in the upper part of the domain boundary, there are no geodesics that go through the lower part of the domain for the reconstruction. For the case with data obtained in the lower part of the domain boundary, there are not many short geodesics during the reconstruction. Nevertheless, we can still produce good reconstruction in regions where geodesics are available.

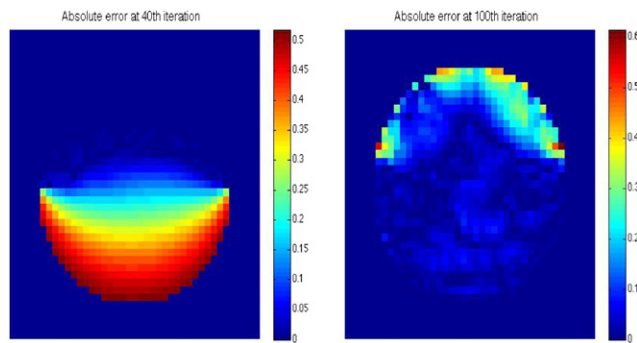


Figure 9. Absolute errors. Left: when data are obtained in the upper-half of the boundary. Right: when data are obtained in the lower-half of the boundary.

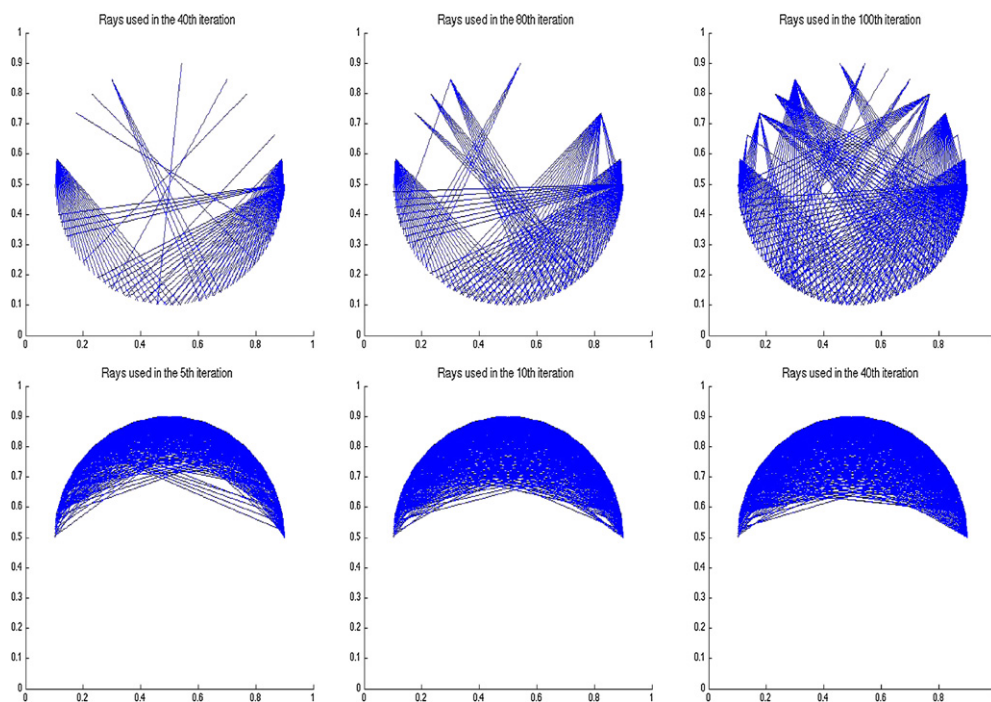


Figure 10. Top: rays used in the 40th, 80th and 100th iterations for measurements obtained on the lower part of the domain. Bottom: rays used in the 5th, 10th and 40th iterations for measurements obtained on the upper part of the domain.

4.5. Example 5: a concave obstacle

In this example, we consider the numerical reconstruction of an unknown medium which contains a known concave obstacle. In this case, some geodesics can have more than one reflections at the obstacle interface, which poses a challenge in the numerical reconstruction.

The exact solution is $c(x, y) = 1 + 0.1 \sin(0.5\pi x) \sin(0.5\pi y)$. The initial guess is $c_0(x, y) = 0.8$. The grid is 30×30 and we use 30 directions at each grid point on the

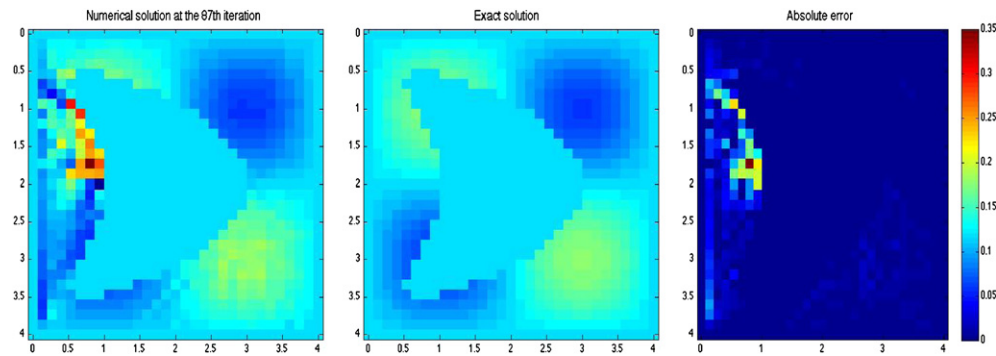


Figure 11. Left: numerical solution at the 117th iteration. The relative error is 2.8%. Middle: exact solution. Right: absolute error.

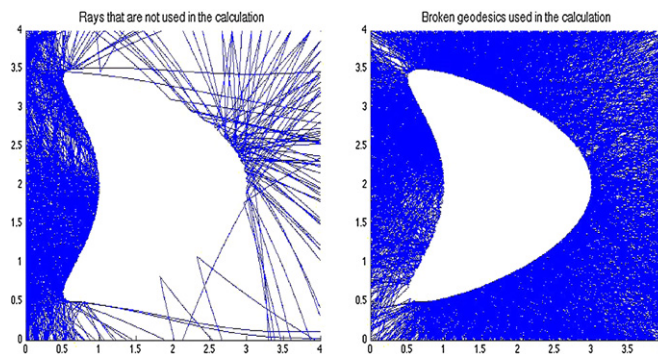


Figure 12. Left: rays not used in the calculation. Right: broken geodesics used in the calculation.

boundary. The regularization parameter is taken as $\beta = 1$. For the parameter in the adaptive approach, we take $\varepsilon = \min(0.5\sigma_n, 1)$.

The inclusion is formed by a concave kite-shaped object with the parametric representation

$$x(t) = \cos(t) + 0.65 \cos(2t) - 0.65, \quad y(t) = 1.5 \cos(t), \quad 0 \leq t \leq 2\pi.$$

In this case, there are geodesics that have four reflections at the interface in our simulation.

Our adaptive numerical algorithm gives a numerical approximation at the 117 iteration with a relative error of 2.8%. Without the adaptive strategy, the phase space method does not even converge for this example. The numerical results are shown in figure 11. In figure 12, we show rays that are not used (left) and broken rays that are used (right) in the calculation. We see that most non-broken rays are used in the final reconstruction and most of the unused rays have reflections in the concave region. As discussed before, the difficulty at the concave region is due to the fact that neither non-broken geodesics nor short broken geodesics can reach the concave region. On the other hand, broken geodesics have to be used to reach the concave region. In the adaptive strategy, after non-broken rays are used to provide a good estimate of the metric outside the convex hull of the concave region, some broken rays are then used to provide the estimate of the metric inside the concave region. Although many broken rays are not used, we still manage to get a pretty good reconstruction in the concave region. By avoiding using those erroneous rays in our adaptive approach, we gain stability. Of course the

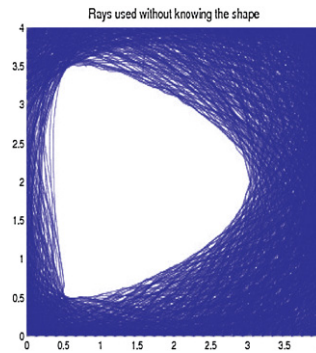


Figure 13. Ray coverage of the unknown obstacle.

tradeoff between accuracy and stability is always a tricky issue. In general, a concave region in reflection tomography poses a great challenge due to multiple reflection or scattering; the more concave the region is, the more difficult it is to reconstruct.

4.6. Example 6: unknown obstacles

In this section, we present a few examples in the most difficult setting in reflection traveltime tomography where both the location of reflection and the underlying medium are unknown. We demonstrate that our adaptive method is able to recover the convex (with respect to the underlying metric) hull of the unknown concave obstacles and the metric outside the convex hull. The key idea is that our adaptive method can distinguish non-broken rays from broken ones in the measurements and use non-broken ones for the reconstruction first. Since we do not know whether there is reflection or not and we do not know the location of the reflection if there is, we cannot use those broken geodesics. Hence, we assume that there is no reflection first. So those rays that are broken will not be used in the reconstruction because the erroneous assumption misses the jump condition at the broken point which will produce a large mismatch with the measurement. Once most non-broken rays are used, we can (1) plot those rays to find the convex hull of the obstacle (if there is one) and (2) reconstruct the metric outside the convex hull.

In the first two examples (figures 13 and 14), we show the recovery of obstacles with an unknown constant velocity field $c(x) = 1$. Then, we will present an example (see figure 15) with a non-constant velocity field enclosing a convex unknown obstacle. In the final example (see figures 16 and 17), we will consider the recovery of both the non-convex unknown obstacle and the unknown non-constant velocity field.

In the first test, we use an unknown obstacle of the concave kite shape as in section 4.5. In figure 13, we show a figure where we draw only those rays that are used in the calculation. We see that the rays give the convex hull of the unknown concave obstacle.

In figure 14, we show another test where there are two unknown concave obstacles. The two obstacles are shown in the left plot of figure 14. In the middle plot of figure 14, we plot the rays that are used in the reconstruction. Again we obtain the convex hull for each of the two obstacles because they are well separated. Moreover, the relative error of the recovered velocity field is only 0.3%.

In figure 15, we show the reconstruction with a convex unknown elliptical object defined by the equation $\frac{(x-0.5)^2}{0.04} + \frac{(y-0.5)^2}{0.09} = 1$. The unknown velocity field is $c(x) = 1 - 0.3e^{-2x^2}$ with

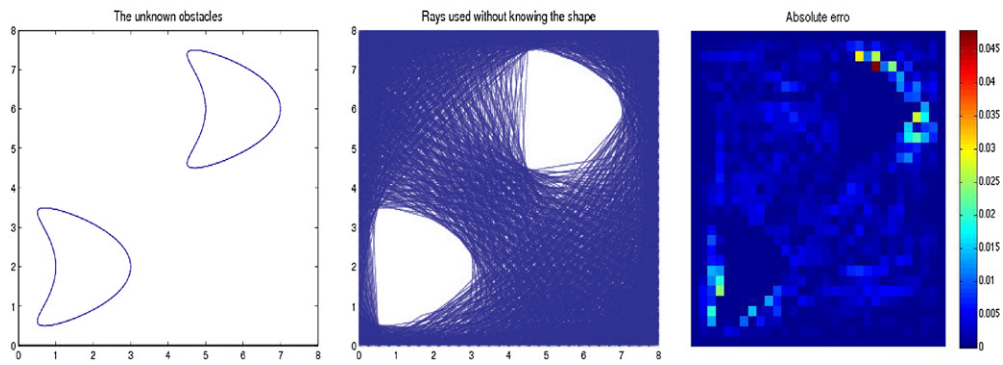


Figure 14. Left: the two unknown obstacles. Middle: ray coverage of the unknown obstacle. Right: absolute error.

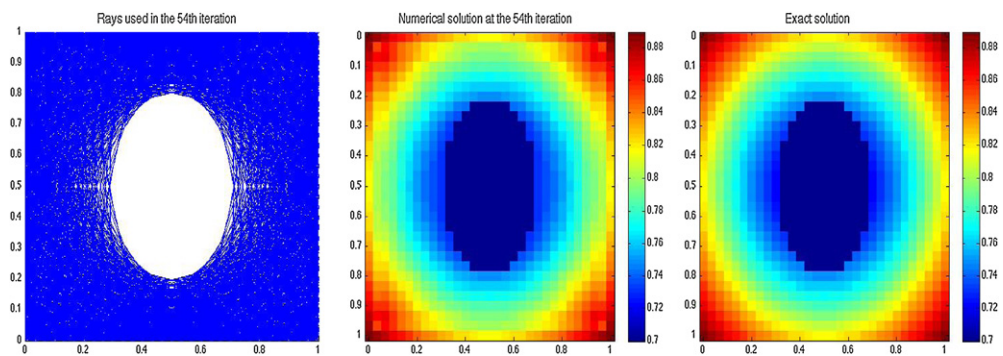


Figure 15. Left: ray coverage of the unknown obstacle. Middle: numerical solution at the 54th iteration. Relative error is 0.3%. Right: exact solution.

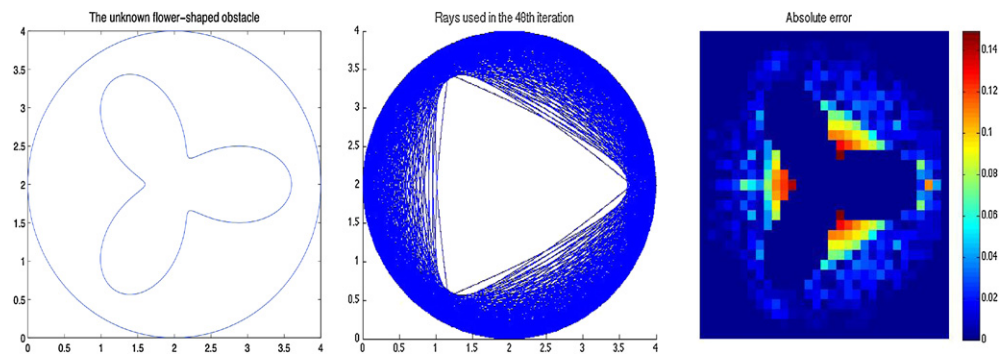


Figure 16. Left: the unknown obstacle. Middle: ray coverage of the unknown obstacle. Right: absolute error.

$r = \sqrt{(x - 0.5)^2 + (y - 0.5)^2}$. In the left plot of figure 15, we present the rays that are used in the calculation. One sees that the coverage of the rays gives an excellent reconstruction of the unknown obstacle. In the middle and right plots of figure 15, we present both the numerical

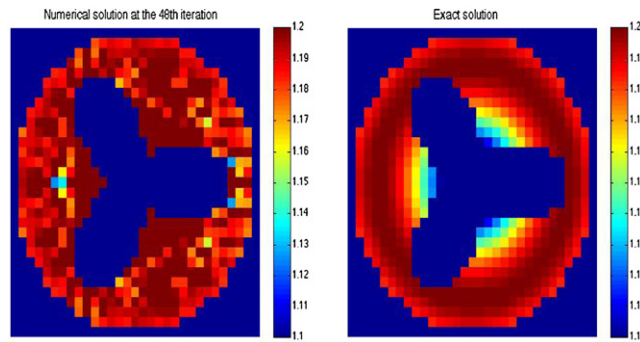


Figure 17. Left: numerical solution at the 48th iteration. Relative error is 2.67%. Right: exact solution.

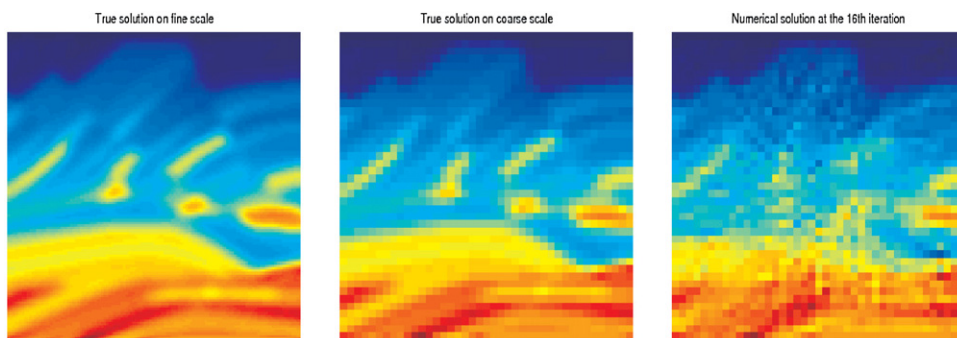


Figure 18. Marmousi model. Left: the exact solution on fine grid. Middle: the exact solution projected on a coarse grid. Right: the numerical solution at the 16th iteration. The relative error is 2.24%.

solution and the exact solution for the velocity field; the corresponding relative error is only 0.3%.

In figure 16, we show the reconstruction with a very concave unknown object of a flower shape $r = 1 + 0.6 \cos(3\theta)$ with $r = \sqrt{(x-2)^2 + (y-2)^2}$. The unknown velocity field is $c(x) = 1 + 0.2 \sin(r)$ with $r = \sqrt{(x-2)^2 + (y-2)^2}$. The unknown obstacle is shown in the left plot of figure 16. In this example, we also take the domain Ω as a circle. In the middle plot of figure 16, we have shown the rays that are used in the calculation. Again we obtain the envelope of the convex hull of the obstacle. The absolute error of the numerical solution is also shown in the right plot of figure 16. We see that we get a good recovery outside the convex hull of the unknown obstacle, which is the region covered by the rays. In figure 17, we present both the numerical solution and the exact solution for the velocity field. The corresponding relative error is 2.67%.

4.7. Example 7: the Marmousi model

In this section, we test our method on a well-known benchmark problem: the Marmousi model. The exact velocity field is defined on a 122×122 grid and is shown in the left plot of figure 18. In our numerical reconstruction, we use a 41×41 grid. We use 50 directions at each

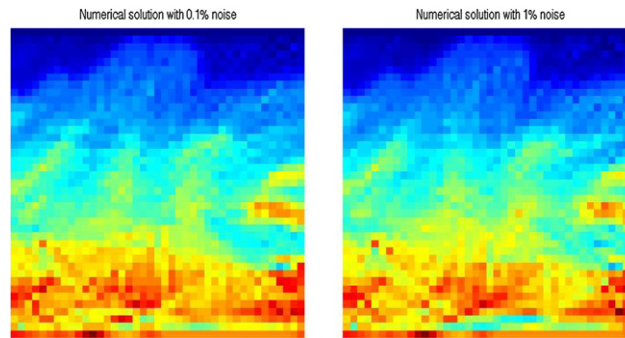


Figure 19. Marmousi model. Left: the numerical solution with 0.1% noise. The relative error is 4.16%. Right: the numerical solution with 1% noise. The relative error is 5.53%.

grid point along the boundary. The regularization parameter $\beta = 100$. We will compare our numerical solution to the exact solution projected on a 41×41 coarse grid, see the middle plot of figure 18. We take the initial guess as $c_0 = 1500$. We use $\varepsilon = \min(0.1\sigma_n, 1)$. The algorithm converges at the 16th iteration with a relative error of 2.24%. In the right plot of figure 18, we have shown the numerical approximation. Comparing to the result we obtained using the original phase space method in [5] for the same problem, the adaptive method is much better

Furthermore, we test the robustness of our numerical algorithm by adding some noise in the data, with the same numerical setting as above except that we take $\beta = 10000$. In figure 19, we present the numerical solutions when the noise levels are 0.1% and 1%, with relative errors 4.16% and 5.53%, respectively. We see that our method behaves quite robustly.

5. Conclusions

In this work, we presented an adaptive phase space method for traveltimes tomography that can deal with multiple arrival times using the scattering relations. Compared to the original method proposed in [5], the adaptive strategy uses more accurate geodesics first and improves the reconstruction gradually in a more stable and efficient way. The proposed adaptive method can also distinguish and utilize broken and non-broken geodesics accordingly for the case of reflection traveltimes tomography.

Acknowledgments

EC is supported by RGC General Research Fund (project no 400609). JQ is supported by NSF 0810104. GU is partly supported by NSF, a Chancellor Professorship at UC Berkeley and a Senior Clay Award. HZ is supported by NSF Grant DMS0811254.

References

- [1] Berryman J 1990 Stable iterative reconstruction algorithm for nonlinear traveltimes tomography *Inverse Problems* **6** 21–42
- [2] Billette F and Lambaré G 1998 Velocity macro-model estimation from seismic reflection data by stereotomography *Geophys. J. Int.* **135** 671–90
- [3] Bishop T N, Bube K P, Cutler R T, Langan R T, Love P L, Resnick J R, Shuey R T, Spindler D A and Wyld H W 1985 Tomographic determination of velocity and depth in laterally varying media *Geophysics* **50** 903–23

- [4] Bube K P and Langan R T 1997 Hybrid l^1 - l^2 minimization with applications to tomography *Geophysics* **62** 1183–95
- [5] Chung E, Qian J, Uhlmann G and Zhao H K 2007 A new phase space method for recovering index of refraction from travel times *Inverse Problems* **23** 309–29
- [6] Chung E, Qian J, Uhlmann G and Zhao H K 2008 A phase-space formulation for elastic-wave traveltimes tomography *J. Phys.: Conf. Ser.* **124** 012018
- [7] Collins M and Kuperman W A 1994 Inverse problems in ocean acoustics *Inverse Problems* **10** 1023–40
- [8] Crandall M G, Evans L C and Lions P L 1984 Some properties of viscosity solutions of Hamilton–Jacobi equations *Trans. Am. Math. Soc.* **282** 487–502
- [9] Crandall M G and Lions P L 1983 Viscosity solutions of Hamilton–Jacobi equations *Trans. Am. Math. Soc.* **277** 1–42
- [10] Crandall M G and Lions P L 1984 Two approximations of solutions of Hamilton–Jacobi equations *Math. Comp.* **43** 1–19
- [11] Dahlen F A, Hung S-H and Nolet G 2000 Frechet kernels for finite-frequency traveltimes—I. Theory *Geophys. J. Int.* **141** 157–74
- [12] Day A J, Peirce C and Sinha M C 2001 Three-dimensional crustal structure and magma chamber geometry at the intermediate-spreading, back-arc Valu Fa Ridge, Lau Basin—results of a wide-angle seismic tomographic inversion *Geophys. J. Int.* **146** 31–52
- [13] Dellinger J and Symes W W 1997 Anisotropic finite-difference traveltimes using a Hamilton–Jacobi solver *67th Ann. Int. Mtg. Soc. Expl. Geophys.: Expanded Abstracts (Tulsa, OK)* 1786–9
- [14] Delprat-Jannaud F and Lailly P 1995 Reflection tomography: how to handle multiple arrivals? *J. Geophys. Res.* **100** 703–15
- [15] Desaubies Y 1990 Ocean acoustic tomography *Oceanography and Geophysical Tomography* ed Y Desaubies, A Tarantola and J Zinn-Justin (Amsterdam: North Holland) pp 203–48
- [16] Fomel S, Luo S and Zhao H K 2009 Fast sweeping method for the factored eikonal equation *J. Comput. Phys.* **228** 6440–55
- [17] Frigiyik B, Stefanov P and Uhlmann G 2008 The x-ray transform for a generic family of curves and weights *J. Geom. Anal.* **18** 89–108
- [18] Gray S 1986 Efficient traveltimes calculations for Kirchhoff migration *Geophysics* **51** 1685–8
- [19] Guillemin V 1976 Sojourn times and asymptotic properties of the scattering matrix *Publ. Res. Inst. Math. Sci. Kyoto Univ.* **12** 69–88
- [20] Harlan W and Burridge R 1983 A tomographic velocity inversion for unstacked data *Stanford Exploration Project* SEP37-01
- [21] Harris J M, Nolen-Hoeksema R C, Langan R T, Van Schaack M, Lazaratos S K and Rector J W III 1995 High-resolution crosswell imaging of a West Texas carbonate reservoir: part I. Project summary and interpretation *Geophysics* **60** 667–81
- [22] Kao C, Osher S and Qian J 2008 Legendre transform based fast sweeping methods for static Hamilton–Jacobi equations on triangulated meshes *J. Comput. Phys.* **227** 10209–25
- [23] Kao C Y, Osher S J and Qian J 2004 Lax–Friedrichs sweeping schemes for static Hamilton–Jacobi equations *J. Comp. Phys.* **196** 367–91
- [24] Kurley Y, Lassas M and Uhlmann G 2010 Rigidity of broken geodesics flow and inverse problems *Am. J. Math.* **132** 529–62
- [25] Leung S and Qian J 2006 An adjoint state method for three-dimensional transmission traveltimes tomography using first-arrivals *Commun. Math. Sci.* **4** 249–66
- [26] Leung S and Qian J 2007 Transmission traveltimes tomography based on paraxial Liouville equations and level set formulations *Inverse Problems* **23** 799–821
- [27] Lions P L 1982 *Generalized Solutions of Hamilton–Jacobi Equations* (Boston, MA: Pitman)
- [28] Liu Z and Bleistein N 1995 Migration velocity analysis: theory and an iterative algorithm *Geophysics* **60** 142–53
- [29] Luo S and Qian J 2011 Factored singularities and high-order Lax–Friedrichs sweeping schemes for point-source traveltimes and amplitudes *J. Comput. Phys.* **230** 4742–55
- [30] May B T and Covey J D 1981 An inverse ray method for computing geologic structures from seismic reflections—zero-offset case *Geophysics* **46** 268–87
- [31] Michel R 1981 Sur la rigidite imposee par la longueur des geodesiques (On the rigidity imposed by the length of geodesics) *Invent. Math.* **65** 71–83 (in French)
- [32] Munk W, Worcester P and Wunsch C 1995 *Ocean Acoustic Tomography* (New York: Cambridge University Press)
- [33] Munk W and Wunsch C 1979 Ocean acoustic tomography: a scheme for large scale monitoring *Deep-Sea Res.* **26A** 123–61

- [34] Nowack R L and Li C 2006 Application of autoregressive extrapolation to the cross-borehole tomography *Studies Geophys. Geod.* **50** 337–48
- [35] Pestov L and Uhlmann G 2004 On characterization of the range and inversion formulas for the geodesic x-ray transform *Int. Math. Res. Not.* **80** 4331–47
- [36] Pestov L and Uhlmann G 2005 Two-dimensional compact simple Riemannian manifolds are boundary distance rigid *Ann. Math.* **161** 1093–110
- [37] Podvin P and Lecomte I 1991 Finite difference computation of traveltimes in very contrasted velocity models: a massively parallel approach and its associated tools *Geophys. J. Int.* **105** 271–84
- [38] Popovici A M and Sethian J A 1997 Three-dimensional traveltime computation using the fast marching method *67th Ann. Int. Mtg. Soc. Expl. Geophys.: Expanded Abstracts (Tulsa, OK)* pp 1778–81
- [39] Qian J and Symes W W 2002 Adaptive finite difference method for traveltime and amplitude *Geophysics* **67** 167–76
- [40] Qian J and Symes W W 2002 Finite-difference quasi-P traveltimes for anisotropic media *Geophysics* **67** 147–55
- [41] Qian J, Zhang Y T and Zhao H K 2007 Fast sweeping methods for eikonal equations on triangulated meshes *SIAM J. Numer. Anal.* **45** 83–107
- [42] Qian J, Zhang Y T and Zhao H K 2007 Fast sweeping methods for static Hamilton–Jacobi equations on triangulated meshes *J. Sci. Comp.* **31** 237–71
- [43] Qin F, Luo Y, Olsen K B, Cai W and Schuster G T 1992 Finite difference solution of the eikonal equation along expanding wavefronts *Geophysics* **57** 478–87
- [44] Romanov V G 1987 *Inverse Problems of Mathematical Physics* (Utrecht: VNU Science Press BV)
- [45] Schneider W A, Ranzinger K, Balch A and Kruse C 1992 A dynamic programming approach to first arrival traveltime computation in media with arbitrarily distributed velocities *Geophysics* **57** 39–50
- [46] Sei A and Symes W W 1994 Gradient calculation of the traveltime cost function without ray tracing *65th Ann. Int. Mtg. Soc. Expl. Geophys.: Expanded Abstracts (Tulsa, OK)* pp 1351–4
- [47] Sei A and Symes W W 1995 Convergent finite-difference traveltime gradient for tomography *66th Ann. Int. Mtg. Soc. Expl. Geophys.: Expanded Abstracts (Tulsa, OK)* pp 1258–61
- [48] Sharafutdinov V A 1994 *Integral Geometry of Tensor Fields* (Utrecht: VSP BV)
- [49] Stefanov P and Uhlmann G 1998 Rigidity for metrics with the same lengths of geodesics *Math. Res. Lett.* **5** 83–96
- [50] Stefanov P and Uhlmann G 2004 Stability estimates for the x-ray transform of tensor fields and boundary rigidity *Duke Math. J.* **123** 445–67
- [51] Stefanov P and Uhlmann G 2005 Boundary rigidity and stability for generic simple metrics *J. Am. Math. Soc.* **18** 975–1003
- [52] Stefanov P and Uhlmann G 2005 Recent progress on the boundary rigidity problem *Electron. Res. Announc. Am. Math. Soc.* **11** 64–70
- [53] Stefanov P and Uhlmann G 2008 Integral geometry of tensor fields on a class of non-simple Riemannian manifolds *Am. J. Math.* **130** 239–68
- [54] Stefanov P and Uhlmann G 2009 Local lens rigidity with incomplete data for a class of non-simple Riemannian manifolds *J. Differ. Geom.* **82** 383–409
- [55] Stefanov P and Uhlmann G 2011 The geodesic x-ray transform with fold caustics *Anal. PDE* at press
- [56] Sword C H 1987 Tomographic determination of interval velocities from reflection seismic data: the method of controlled directional reception *PhD Thesis* Stanford University, Stanford, CA
- [57] Taillandier C, Noble M and Calandra H 2008 A massively parallel 3D refraction traveltime tomography algorithm *70th EAGE Conference and Exhibition* pp 1–5
- [58] Taillandier C, Noble M, Chauris H, Podvin P, Calandra H and Guilbot J 2007 Refraction traveltime tomography based on adjoint state techniques *69th EAGE Conf. and Exhibition* pp 1–5
- [59] Tsai R, Cheng L-T, Osher S J and Zhao H K 2003 Fast sweeping method for a class of Hamilton–Jacobi equations *SIAM J. Numer. Anal.* **41** 673–94
- [60] van Trier J and Symes W W 1991 Upwind finite-difference calculations of traveltimes *Geophysics* **56** 812–21
- [61] Vidale J 1988 Finite-difference calculation of travel times *Bull. Seis. Soc. Am.* **78** 2062–76
- [62] Washbourne J K, Rector J W and Bube K P 2002 Crosswell traveltime tomography in three dimensions *Geophysics* **67** 853–71
- [63] Zelt C A and Barton P J 1998 Three-dimensional seismic refraction tomography: a comparison of two methods applied to data from the Faeroe Basin *J. Geophys. Res.* **103** 7187–210
- [64] Zhao H K 2005 Fast sweeping method for eikonal equations *Math. Comp.* **74** 603–27